Electrochimica Acta 549 (2026) 148026

Contents lists available at ScienceDirect

Electrochimica Acta

journal homepage: www.journals.elsevier.com/electrochimica-acta

Evolution of macrocell and microcell corrosion in concrete subjected to simulated tiding

Miha Hren *, Tadeja Kosec, Andraž Legat

Slovenian National Building and Civil Engineering Institute, Slovenia

ARTICLE INFO

Keywords:
Corrosion
Coupled multi-electrodes (CMEs)
Simulated tiding
Reinforced concrete
Macrocell corrosion

ABSTRACT

The aim of this study was to investigate the interaction between macrocell and microcell corrosion processes in a concrete column exposed to tidal conditions simulated by sinusoidal water-level changes. Macrocell corrosion currents were continuously measured for 19 weeks along the column height using coupled multi-electrodes (CMEs). Cumulative corrosion damage and the morphology of corrosion products were analysed using X-ray microCT, SEM, and Raman spectroscopy. The results showed complex patterns of anodic and cathodic activity, including sinusoidal and switch-like current behaviour, which depended on the water level position and exposure time. Corrosion typically initiated in the upper tidal zone, but the most corroded individual electrode was located near mid-tide. Damage distribution was influenced by both microcell and macrocell corrosion, where microcell corrosion was most prevalent in the high-tide area, whereas macrocell activity contributed to corrosion damage in several exposure zones. SEM and Raman analyses confirmed a correlation between corrosion type and corrosion product morphology. An attempt was made to explain the recognised corrosion patterns along the vertical position and the ratios between microcell and macrocell corrosion on individual electrodes were estimated. Additionally, new questions were raised that highlight the complexity of corrosion processes under tidal cycling and emphasise the need for further research into these phenomena.

Introduction

Reinforced concrete structures were long considered durable, as the alkalinity of the concrete provides a passive environment for the embedded steel [1]. Even if such structures are well designed and constructed, depassivation of the carbon steel reinforcement can occur due to carbonation of the concrete and/or the ingress of aggressive species, usually chlorides [1–3]. Corrosion processes are initiated under these conditions, causing a reduction in the cross-section and significantly reducing the service life of the reinforced structure as a result [1,2]. These concerns have motivated extensive research into corrosion initiation and corrosion propagation of steel reinforcement in concrete.

Corrosion in reinforced concrete is unique because anodic and cathodic reactions can occur at spatially separated locations within the cementitious matrix. Unlike in aqueous electrolytes, small anodic “hot spots” can develop in concrete and couple with distant cathodic regions [4]. The relatively large dimensions of reinforced concrete elements can therefore support considerable distances between anodic and cathodic sites [4]. In such cases, anodic corrosion processes can occur very locally, damaging only a few square centimetres of the steel surface, while large neighbouring areas of the steel surface remain passive [5]. This indicates a clear separation of the anodic and cathodic reactions, leading to the formation of a macrocell. Simultaneously, numerous adjacent anodic and cathodic sites may form on a microscale due to steel heterogeneity and local chemistry, producing microcell corrosion (also called self-corrosion) [6]. Both macrocell and microcell processes typically operate together, with localised anodes driving long-range currents even as microcell corrosion occurs elsewhere on the steel surface [7].

The intensity of macrocell corrosion depends strongly on the geometry and material properties of the reinforced concrete structure. Among the major influencing factors are the cathode-to-anode area ratio, separation distance, and concrete resistivity[8]. Larger cathodic areas accelerate macrocell current by providing a greater area for oxygen reduction, while a greater anode-to-cathode distance reduces current due to the IR drop in concrete [8]. Concrete resistivity is equally influential. Low-resistivity concrete enables long-distance coupling, whereas high-resistivity concrete only allows for short-distance galvanic interactions.

Abbreviations: CME, Coupled multi-electrode; CMEA, Coupled multi-electrode array; ZRA, Zero resistance ammeter; OPC, Ordinary Portland cement.

* Corresponding author.
E-mail address: miha.hren@zag.si (M. Hren).

https://doi.org/10.1016/j.electacta.2025.148026
Received 3 October 2025; Received in revised form 28 November 2025; Accepted 15 December 2025
Available online 16 December 2025

Chalhoub et al. [9] showed that anodes in large elements can draw current from cathodes metres away if resistivity is low, but this reach diminishes sharply as resistivity increases [9]. Where multiple cathodes are present, the nearest cathode supplies most of the macrocell current. This effect is intensified by higher resistivity [9]. Therefore, strategies that increase resistivity or limit large cathode-to-anode area ratios, such as using dense concretes with low permeability, can significantly mitigate macrocell corrosion. Ultra-high-performance concretes, for example, exhibit almost no macrocell activity due to their high resistivity and low oxygen diffusivity [8].

Despite the prevalence of macrocell corrosion, conventional electrochemical techniques are not able to distinguish it from microcell processes. Methods such as half-cell mapping, linear polarization resistance, electrochemical impedance spectroscopy, and galvanostatic pulse technique provide only combined signals from all concurrent corrosion reactions [10–13]. These methods, based on mixed-potential theory [14,15], cannot determine whether measured corrosion currents originate from a localised anodic patch (macrocell) or from general uniform corrosion (microcells) [16]. The interpretation of electrochemical measurements is mainly complicated by the heterogeneous structure of concrete, which affects oxygen availability, pore solution connectivity, and is responsible for various localised features on the steel–concrete interface [17]. Environmental factors such as wetting and drying, rainfall, temperature changes, or tidal cycling can further influence corrosion behaviour, which periodic measurements may miss [18]. As Angst and Büchler [19] noted, researchers can reach misleading conclusions if Stern–Geary-based corrosion rates are estimated when macrocell currents are also present. These challenges have led to the use of alternative methods to monitor corrosion processes in concrete over space and time [6,20–25].

Among advanced techniques, coupled multi-electrode arrays (CMEA or CME) are commonly used to map corrosion activity over time. Small steel electrodes are embedded in concrete and electrically coupled through a system of zero-resistance ammeters (ZRAs), allowing measurement of current exchange between them [26]. At any time, electrodes can behave as either anodes or cathodes, revealing where, when, and what type of corrosion processes are occurring [27]. As electrode polarity can change due to corrosion progression, CMEAs provide continuous spatio-temporal corrosion measurements. This capability is particularly valuable for investigating macrocell corrosion, where anodic and cathodic sites may be centimetres apart. CMEAs have been used to observe how localised anodic sites develop in chloride-rich zones and draw balancing cathodic currents from surrounding electrodes [28] They can also quantify localised corrosion rates and track damage accumulation at anodic areas [29].

Electrical resistance (ER) sensors provide a complementary means of tracking corrosion progress by measuring cross-sectional loss of a metal electrode embedded in concrete [25]. As the electrode corrodes, its electrical resistance increases [30]. Although ER probes primarily record total corrosion loss rather than separating macrocell and microcell effects, multi-electrode systems can reveal differential corrosion trends or be configured to detect galvanic corrosion [28,31].

X-ray micro-computed tomography (microCT) is a powerful imaging tool for visualising internal corrosion damage in a non-destructive way. MicroCT can be used to identify localised corrosion damage, quantify material loss due to corrosion, and visualise cracks around corroding reinforcement [11,23,26,32–36]. It also enables post-exposure validation of electrochemical measurements, as it can separately detect uncorroded steel, corrosion products, voids, cracks, and other features at the steel–concrete interface. MicroCT and electrochemical measurements have already been used to correlate macrocell currents with localised damage and corrosion product formation [37]. Such multi-technique approaches are increasingly considered beneficial for interpreting complex corrosion patterns in concrete [28,38].

Due to the high concentrations of chlorides and varying exposure conditions, the marine environment is among the most aggressive for the corrosion of steel in reinforced concrete structures [31,39]. Coastal structures are generally divided into different exposure zones: submerged, tidal, splash, and atmospheric [39,40]. Field studies consistently show that the splash zone is the most corrosive, followed by the tidal zone, while fully submerged and atmospheric zones are less prone to corrosion [41]. This variability in behaviour results from differences in chloride and oxygen availability. The splash and tidal zones have abundant chlorides and are periodically oxygenated, whereas the submerged zone lacks oxygen supply and the atmospheric zone is limited in chlorides [42]. Due to this interaction between chlorides and oxygen, macrocell corrosion is the most likely cause of the corrosion damage gradients observed in marine structures [16]. Differential aeration between submerged anoxic steel and higher, oxygen-rich steel can create strong macrocells, where submerged or partly submerged steel becomes anodic and higher positioned steel becomes cathodic [8]. This mechanism is similar to corrosion at the soil–air interface of buried pipelines [8]. Such long-range galvanic effects may help explain the greater damage observed in tidal and splash zones.

To improve consistency across marine exposure studies, RILEM TC 289-DCM has published state-of-the-art reviews and guidelines for the design and operation of marine exposure sites [43,44]. These recommendations cover exposure site selection, specimen placement and orientation, environmental monitoring, and standardised data reporting, with the goal of enabling more reliable comparisons of corrosion performance worldwide. Nevertheless, significant knowledge gaps remain, particularly regarding corrosion initiation and corrosion propagation in the tidal and splash zones under changing wetting conditions.

Recently some studies have been done where the effects of macrocell corrosion was researched under simulated marine conditions. Lliso-Ferrando et al. [16] exposed partially submerged reinforced concrete columns and found that macrocell currents increased steel loss by factors of 3 to 8 compared to microcell corrosion. The submerged steel acted as the anode, while the drier area behaved cathodically. However, their setup used static water levels, without cyclic tiding. Bui and Tan [45] introduced wet-dry cycles to simulate tidal or splash exposure and found that macrocell currents increased during drying, which accelerated corrosion beyond what was measured under continuously wet conditions. Their findings emphasise that macrocell corrosion is highly dynamic and sensitive to cyclic exposure. Liu et al. [41], on the other hand, used modelling to simulate non-uniform marine corrosion. Their model predicted significant macrocell activity between various exposure zones.

A previous field study using multiple complementary monitoring techniques also investigated these processes by exposing large reinforced concrete columns to a natural marine environment for over four years [31]. ER probes were used to monitor microcell corrosion rates at different depths, while CME electrodes were used to monitor macrocell currents. The authors noted that the large electrode spacing and surface area allowed macrocell and microcell corrosion to occur simultaneously on each electrode, producing cumulative damage that was difficult to interpret. Additionally, natural exposure conditions made it difficult to distinguish between exposure zones (submerged, tidal, and splash), as sensors were subjected to a combination of wetting from tides, waves, water spray, and rainfall. As a result, the contribution of macrocell and microcell corrosion could not be accurately quantified. Carbon steel exhibited the highest corrosion damage in splash and tidal zones, while stainless steel remained largely undamaged, consistent with previously discussed literature.

The aim of this study is to address the uncertainties of previous works. To this end, we designed a controlled laboratory experiment to monitor macrocell corrosion under dynamic sinusoidal tidal conditions. A 1.5 m reinforced concrete column was cast and exposed to a simulated tidal environment for 19 weeks. The corrosion processes were monitored using coupled multi-electrodes (CMEs) embedded along the column height, allowing us to track the evolution of anodic and cathodic sites. Special attention was given to the distribution of macrocell and microcell corrosion over the height of the column and its dynamic

changes. After the 19-week exposure, the embedded steel electrodes were removed and examined using X-ray computed tomography (microCT) and SEM to quantify corrosion damage and characterise corrosion products. Raman spectroscopy was also used to determine the composition of corrosion products. By combining CME measurements with post-exposure analysis, this study aims to clarify how macrocell and microcell corrosion develop over time and influence damage progression under cyclic tiding. It was expected that the combination of all results would help to explain specific details of the corrosion processes at both micro and macro levels under dynamic conditions.

Materials and methods

Specimen design and preparation

A custom-made reinforced concrete column (Fig. 1a) was designed, spanning 1500 mm × 80 mm × 80 mm in dimension. The goal of such design was to simulate a galvanically coupled rebar, where anodic and cathodic sites form due to cyclic tiding. If the measured anodic and cathodic currents occur on different electrodes, it is considered as macrocell corrosion, and if they occur on the same electrode, it is considered as microcell corrosion. To achieve this goal, 12 coupled multi-electrodes were embedded along the height of the column, with a distance of 100 mm between each electrode (Fig. 1b). CME electrodes were made from smooth rebar with a 6 mm diameter, where only the cross-section of the electrodes was exposed (0.28 cm^2). Electrodes were embedded in epoxy resin and polished with 1200 grit paper, following the procedure used for metallurgical samples. A cable wire was soldered to the back of each electrode, and the solder joint was also embedded in epoxy resin for protection. The cables were then connected to a system of ZRAs, as shown in Fig. 1c. Throughout the exposure, the electrodes were galvanically coupled through a system of Zero Resistance Ammeters (ZRAs). The connections of the ZRAs to the electrodes and a common floating ground is schematically shown on Fig. 1c. The electrodes were held in place by a plexiglass holder, where epoxy resin was used to solidify their position and protect the side of the electrodes so that only the cross-section was exposed. In addition to the electrodes, vertical smooth bars (Ø 6 mm) with stirrups were positioned in each corner of the column to provide structural stability.

The vertical bars and CME electrodes were made from smooth carbon steel rods (S235JR). The vertical bars were embedded in their as-received state, with no visible mill scale. The steel rods used for CME electrodes were embedded in epoxy across their cross-section and ground with P1200 grit paper.

The concrete in the column was made from cement CEM I 42,5 N. The cement was obtained from the Anhovo cement factory (Anhovo, Slovenia), and is referred to throughout the rest of the paper by its shorthand designations, CEM I. Table 1 shows the mineral compositions of the cement, which was already presented in a previous study [46]. A water-to-cement ratio of 0.75 was used with a cement-to-aggregate ratio of 1:3. The high water-to-cement ratio was chosen to increase the porosity of the concrete and thus result in faster chloride penetration. Since this approach accelerates corrosion processes, the initiation times may not reflect real-world structures. All the electrodes and smooth bars had a concrete cover of 10 mm. Consequently, a maximum aggregate grain size of 4 mm was chosen. After demoulding, the specimen was stored in a climate-controlled chamber at 20 ± 2 °C and ~100 % RH for 28 days until the time of testing, ensuring a high and stable degree of hydration prior to chloride exposure. The conditions in the chamber were maintained according to SIST EN 12,390–2:2019 [47] standard for making and curing specimens for concrete strength testing.

Simulated environment exposure

The column was exposed to tiding with a 3.5 % NaCl solution at a laboratory test site, which is pictured in Fig. 1a. Prior to the start of the exposure, the barrels containing the specimen and the excess solution were covered with a lid and foil to minimise evaporation during the exposure. The total exposure time was 19 weeks, with 11 weeks of cyclic wetting and 8 weeks of drying. A system of pumps, pressure sensors and Arduinos were used to precisely control the changes in water level over time. The pumps were regulated using custom Arduino code, which continuously adjusted pump power based on real-time measured water level. Water level was monitored using an underwater pressure sensor with a 0–100 mbar range and an accuracy of 1 mbar, corresponding to a water-level calibration uncertainty of approximately ±10 mm. The Arduino code implemented a feedback control routine, increasing or decreasing pump output in proportion to the deviation between the target and current water level. The column was positioned such that the 3 top electrodes were always in the atmospheric zone, 3 bottom electrodes were always in the submerged zone, and the 6 middle electrodes were exposed to cyclic tide simulation (Fig. 1d). The various zones were defined as follows, according to [44]:

- atmospheric zone, which was never directly immersed in the NaCl solution due to water level changes (CME electrodes 1, 2, 3),
- upper and lower tidal zone, where wetting and drying occurred due to changes in the level of the NaCl solution (CME electrodes 4 to 9),

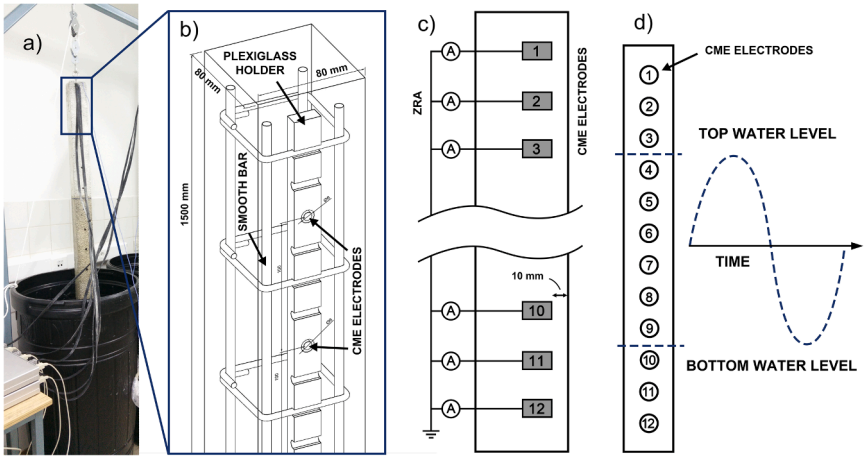

Fig. 1. (a) The entire experimental setup, where the column is lifted into the air. (b) Position of the CME sensors, plexiglass holder, smooth bars and stirrups. (c) Schematic representation of a side view of embedded electrodes connected to ZRAs and a common floating ground. (d) Electrode labels, top and bottom water levels and sinusoidal water level change over time.

Table 1
Mineral composition of cements (in weight %), obtained with X-ray diffraction [46].

Cement	C_3S	C_2S	C_3A	C_4AF	$CaCO_3$	$CaSO_4$ $2H_2O$	SiO_2	Amorphous phase	Other
CEM I	56.8	19.7	7.5	10.4	0.9	1.8	-	0.8	2.1

- submerged zone, which was constantly exposed to the NaCl solution (CME electrodes 10, 11, 12).

Fig. 1d shows the top and bottom water level relative to the position of the electrodes, as well as the sinusoidal water level change over time. The maximum water level during tidal cycling was positioned exactly at the midpoint between electrodes 3 and 4, while the minimum water level was positioned at the midpoint between electrodes 9 and 10. The total water level change was 600 mm. Table 2 shows wet and dry exposure durations (in hours) for each electrode position under the 3-hour and 12-hour tidal cycles. The times were calculated based on the water level position and do not take capillary water suction into account.

Two different periods were used for a full tidal cycle (rise and fall of water level): 3 h and 12 h. At the end of the exposure, the column was left to airdry. The corrosion activity was still monitored during this period to see how anodic and cathodic reactions behave after no additional wetting is applied to the columns. An ambient air temperature of 24 ± 2 °C and a relative humidity of 50±5 % was maintained throughout the exposure.

Coupled multi-electrode technique

The CME technique measures anodic and cathodic currents between galvanically-coupled electrodes. This is achieved by connecting all the exposed electrodes through a system of zero resistance ammeters (ZRAs) [23,25]. The anodic and cathodic currents were measured continuously with a frequency of 1 Hz. The resolution (smallest detectable change in corrosion current density) of the measurement was 1.1 nA/cm^2, a value that already includes the inherent noise characteristics of the system. Positive currents represent anodic activity, while negative currents represent cathodic activity. The measured anodic corrosion current densities (j_{corr} in μA/cm^2) were also converted to corrosion rates (v_{corr} in μm/year) using Eq. (1) [48]. An assumption was made here that the corrosion damage was equally distributed across the entire exposed surface area of the electrode (0.28 cm^2). The following constants were used in the equation: molar mass $M = 55.8$ g/mole, density $\rho = 7.85$ g/cm^3, oxidation number $z = 2$, and a constant of 3.27 in μm g/μA cm year, obtained from Faradays Law.

$$v_{corr} = \frac{3.27M}{\rho\, z} j_{corr} \quad (1)$$

For clarity in data presentation, the raw data was downsampled before plotting. The full-duration plots (19 weeks) were averaged over 100-second intervals, while the higher-resolution, short-duration plots (scaled in hours) were averaged over 10-second intervals.

Table 2
Wet and dry exposure durations (in hours) for each electrode position under the 3- hour and 12- hour tidal cycles.

	3-hour cycle		12- hour cycle	
Electrode	Wetting (h)	Drying (h)	Wetting (h)	Drying (h)
1	0.00	3.00	0.00	12.0
2	0.00	3.00	0.00	12.0
3	0.00	3.00	0.00	12.0
4	0.56	2.44	2.24	9.76
5	1.00	2.00	4.00	8.00
6	1.34	1.66	5.36	6.64
7	1.66	1.34	6.64	5.36
8	2.00	1.00	8.00	4.00
9	2.44	0.56	9.76	2.24
10	3.00	0.00	12.0	0.00
11	3.00	0.00	12.0	0.00
12	3.00	0.00	12.0	0.00

Post-exposure analysis

In addition to visual inspection, all CME electrodes were scanned using the microCT technique at 150 kV and 10 W, using a macro-objective with 0.39× magnification. The device used was an Xradia MicroXCT-400 microCT scanner. A High Energy #1 filter was used, and the spatial resolution obtained was 8.2 μm per voxel. To achieve the highest possible resolution, electrodes were only scanned around the parts that were damaged. The CT results were analysed using Dragonfly 2024.1 software. The scanned volume of each damaged electrode was subtracted from that of the reference electrode (full cylinder) in order to obtain the total corroded volume (in μm^3). Average corrosion depth was obtained by dividing the corroded volume with the exposed surface of the electrode.

Corrosion products on select electrodes were analysed after the exposure with SEM and Raman techniques. A JEOL JSM-IT500 SEM with EDS analyser was used to visualise the corrosion products, while the Raman spectra were obtained with a Horiba Jobin Yvon LabRAM HR800 Raman spectrometer coupled to an optical microscope Olympus BXFM. The measurements were performed using a 632 nm laser excitation line, a 100 × objective lens and a 600 grooves/mm grating, which gave a spectral resolution of 2 cm^{-1}/pixel. A multi-channel CCD detector was used, with integration times between 20 and 35 s. The spectra presented are without baseline correction.

Chloride concentration at the rebar depth and at different exposure zones and different electrode positions (3, 5, 7, 9, 10 and 12) was obtained by drilling cylindrical discs 60 mm in diameter and a height of about 5 mm. This was repeated until rebar depth (10 mm) was reached. The last cylinder, closest to the rebar depth, was ground and used to determine the chloride concentration. The chloride concentration was determined using a leaching method according to SIST EN 14,629:2007 standard [49,50], where acid- and water-soluble chlorides are extracted from the powdered concrete samples. The extracted chlorides were analysed using titration, which allowed us to obtain the total chloride contents at the rebar depth.

Results

Coupled multi-electrodes

Overview of the entire exposure

Coupled multi-electrodes were used to monitor anodic and cathodic currents on 12 positions along a column exposed to cyclic tiding. The complete measurement of the coupled multi-electrodes (CMEs) for the CEM I column is presented in Fig. 2. Electrodes are identified by unique colours and labels from 1 to 12, top to bottom. Positive corrosion density values represent anodic currents, while negative values represent cathodic currents. The graph shows 3 periods of tiding: 3-hour cyclic periods, 12-hour cyclic periods and the drying period. In all 3 exposure periods, sections A, B, C, D and E are labelled, which represent sections that are observed in greater detail (Figs. 4, 5, 6 and 7). The right side of Fig. 2 shows a colour matrix of the electrodes, where the two dashed lines show the area where the tiding took place.

The results show that the corrosion rates were low (~30 nA/cm^2, section A) up until the end of week 6, which was labelled as the corrosion incubation stage. In week 7, corrosion activity increased

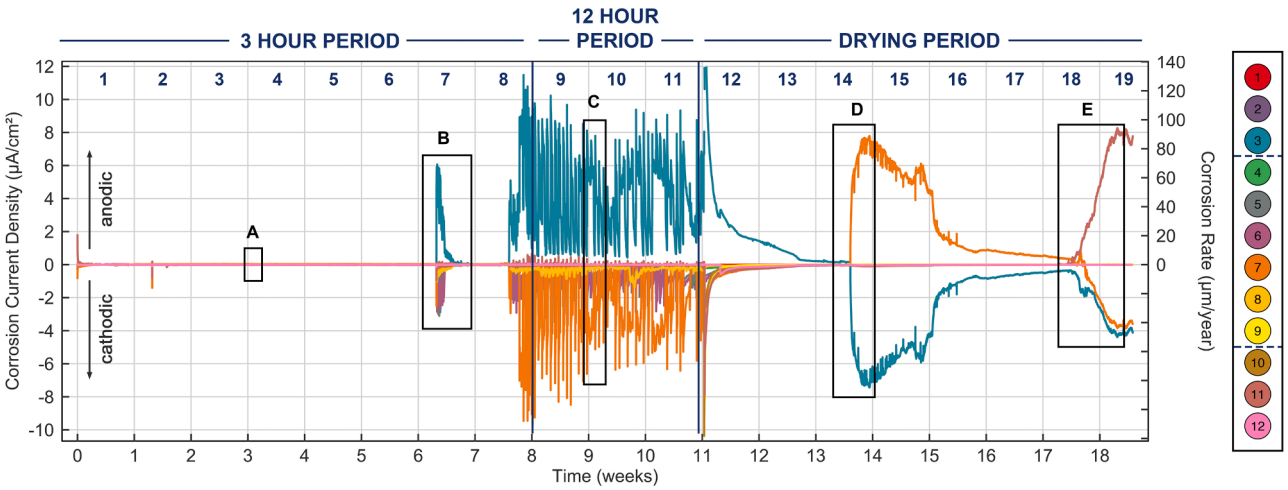

Fig. 2. Corrosion current densities measured on the 12 electrodes of the column specimen. Exposure periods (3-hour, 12 h or drying period) are labelled at the top, while electrode colours and labels are shown on the right. Sections A, B, C and D represent regions of interest that are looked at in greater detail.

significantly, up to 6 μA/cm^2 on electrode 3 in the atmospheric zone (section B). Although the corrosion activity stabilised within the same week, it started corroding again in the middle of week 8, right before the 12-hour cyclic exposure started. Weeks 7 up to the middle of week 8 were labelled as the corrosion initiation stage. Once the 12-hour cyclic period began, the corrosion activity continued at the same amplitude (around 8 μA/cm^2), but the current fluctuations were slower due to the lower frequency of water level changes. This activity continued up until the drying period. Once the columns were left to airdry starting with week 12, corrosion rates increased slightly, and then slowly started decreasing up until week 14, where they again increased rapidly. Localised anodic reactions during the drying period were detected first on electrode 3 (atmospheric zone), then on electrode 7 (tidal zone) and last on electrode 11 (submerged zone). The period from the middle of week 8 to the end of the exposure was described as active corrosion.

In addition to the temporal representation of the CME measurements (Fig. 2), average anodic and cathodic corrosion currents during each exposure period are presented in array form in Fig. 3. Left columns in

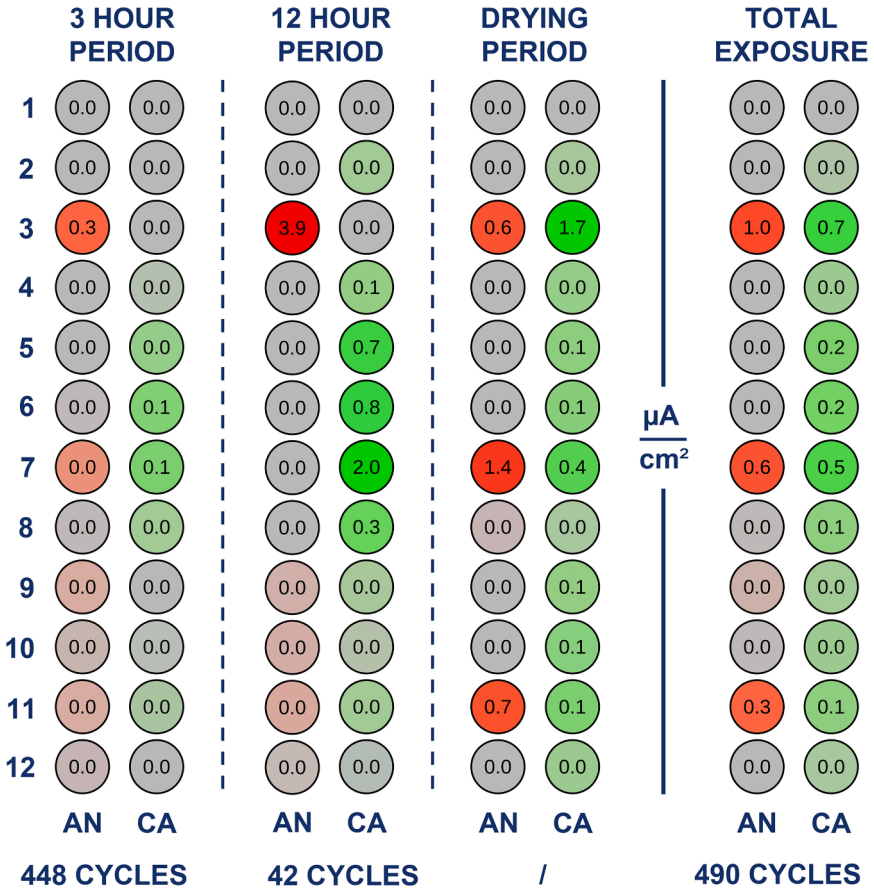

Fig. 3. Average anodic and cathodic corrosion currents (μA/cm^2) during each exposure period. Left columns in each pair represent anodic currents (labelled AN, red colour), while right columns in each pair represent cathodic currents (labelled CA, green colour). Number of tiding cycles are labelled for each exposure period.

each pair represent anodic currents (labelled AN, red colour), while right columns in each pair represent cathodic currents (labelled CA, green colour). During the 3-hour and 12-hour cyclic periods, the electrodes in position 3 (above the upper tidal zone) were the most anodic on average, while the cathodic reaction mainly took place in the tidal zone (electrodes 4 to 9). The average anodic and cathodic reactions were an order of magnitude higher in the 12-hour period (e.g., 3.9 μA/cm^2 on electrode 3) compared to the 3-hour period (e.g., 0.3 μA/cm^2 on electrode 3) due to active corrosion starting towards the end of the 3-hour exposure period. During the drying period, the anodic and cathodic reactions were located predominantly on electrodes 3, 7 and 11, while other electrodes displayed only light cathodic activity. Average anodic and cathodic activity per electrode was lower compared to the 12-hour period, as the 3 electrodes were each active only for a portion of the drying period.

Exposure during the 3-hour period

Figs. 4 and 5 show detailed temporal and spatial changes in anodic and cathodic corrosion currents, which were taken from sections labelled A and B in Fig. 2. Each figure consists of a detailed graph (top left) representing anodic and cathodic current density changes during the wetting cycle, with a synchronised water level change in the bottom left. The graph is covered by 4 lines labelled L (low), M↑ (middle increasing), M↓ (middle decreasing) and H (high). These lines represent points in time where the tide level is at lowest position (0 mm, 3 electrodes submerged), middle position (300 mm, 6 electrodes submerged) or highest position (600 mm, 9 electrodes submerged). The anodic and cathodic currents at each of these points in time are plotted on the right side of each figure.

Fig. 4 represents the corrosion incubation stage (corrosion rates are below 1 μm/year) and was taken from section A in Fig. 2. The detailed graph represents anodic and cathodic changes during the 3-hour tiding cycle. Throughout this period, the most anodic location remains on electrode 7, while the most cathodic location is located on electrode 11 that is constantly submerged. As the water level increases towards the highest position (H), electrodes immediately above electrode 7 become slightly more cathodic, while the cathodic reaction on electrode 11 remains constant. The anodic reaction is highest (between 30 and 40 nA/cm^2) near the peak (H) water level position, with negligible phase shift, while the cathodic reaction on electrode 11 is the highest (between −20 and −30 nA/cm^2) around the middle water level position.

Figs. 5 represents the corrosion initiation stage (section B in Fig. 2) during the 3-hour tiding period. The results show that electrodes below the middle water level position (electrodes 7 to 12) barely participated in the current exchange, and most corrosion activity occurred between electrodes 3 to 6, where there is more oxygen access. Throughout the initiation, electrode 3 remained anodic, having the highest value (5.4 μA/cm^2) as the tide transitioned from lowest to highest position (M↑). Both anodic and cathodic currents were the lowest at the maximum water level (H) and minimum water level (L), indicating a 2-times increase in oscillation frequency from the tidal position. Electrodes 5 and 6 were consistently cathodic throughout the observed period, hovering between –1 μA/cm^2 and –3 μA/cm^2.

Exposure during the 12-hour period

After the 3-hour period and the start of active corrosion, the exposure was switched to 12-hour period to see if the extended drying time and slower wetting time affects the positions of the anodic and cathodic currents, as well as their maximum and minimum fluctuations. The results of a typical tiding cycle are presented in Fig. 6, which was taken from section C in Fig. 2. As previously, each figure consists of a detailed graph (top left) representing anodic and cathodic current density changes during the wetting cycle, with a synchronised water level change in the bottom left. The graph is covered by 4 lines labelled L, M↑, M↓ and H. These lines represent points in time where the tide level is at lowest (L), middle (M↑, M↓) or highest (H) position. The anodic and cathodic currents at each of these points in time are plotted on the right side of each figure.

The results show that electrode 3 (located above the highest water level position) has the highest anodic corrosion activity, while areas below electrode 7 have negligible participation in the current exchange. Both anodic and cathodic activities are highest when the water level is at the lowest position (L), indicating that drying period plays a large role in increasing corrosion activity. Electrodes 1 to 9 were all in the middle of their drying period at this water level position (Table 2). By comparison, when the water level reaches the highest position and slowly descends towards the middle (M↓), the lowest corrosion activities are recorded (+1 μA/cm^2 for anodic and −0.3 μA/cm^2 for cathodic). This indicates that high water saturation and low oxygen presence prevents intense corrosion activity. The phase shift observed during the 12-hour cycle was about 180°

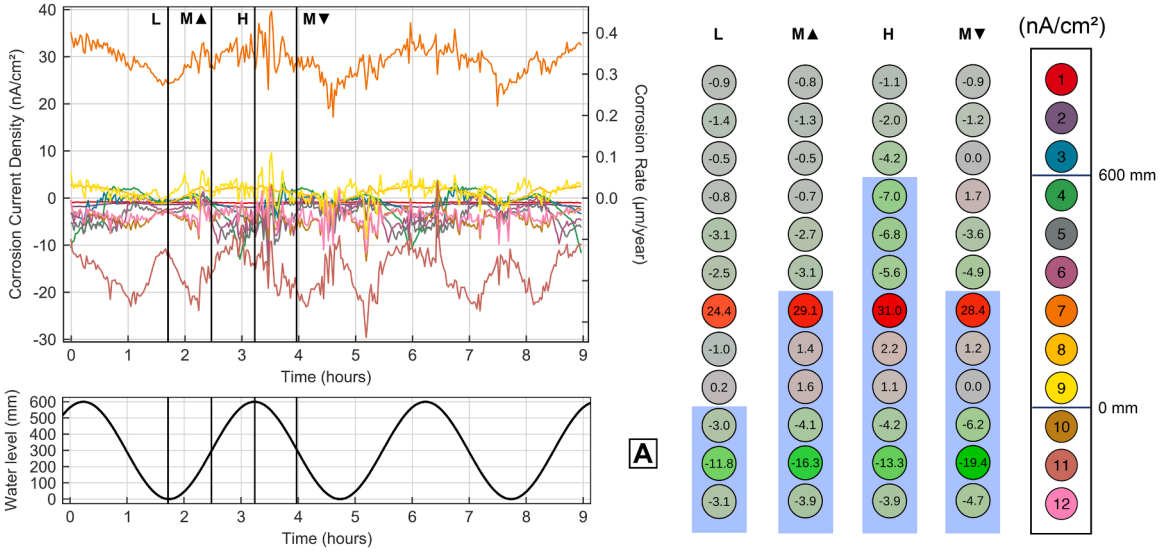

Fig. 4. Corrosion current densities on the column during the 3-hour cyclic period in the corrosion incubation stage. Water level is displayed below the corrosion current density graph, and lines labelled L, M↑, M↓ and H represent the 4 characteristic states of water level: the bottom position (L), middle positions (M↑ and M↓) and top position (H). On the right side of the graph, anodic and cathodic currents for each of these states are presented in array form.

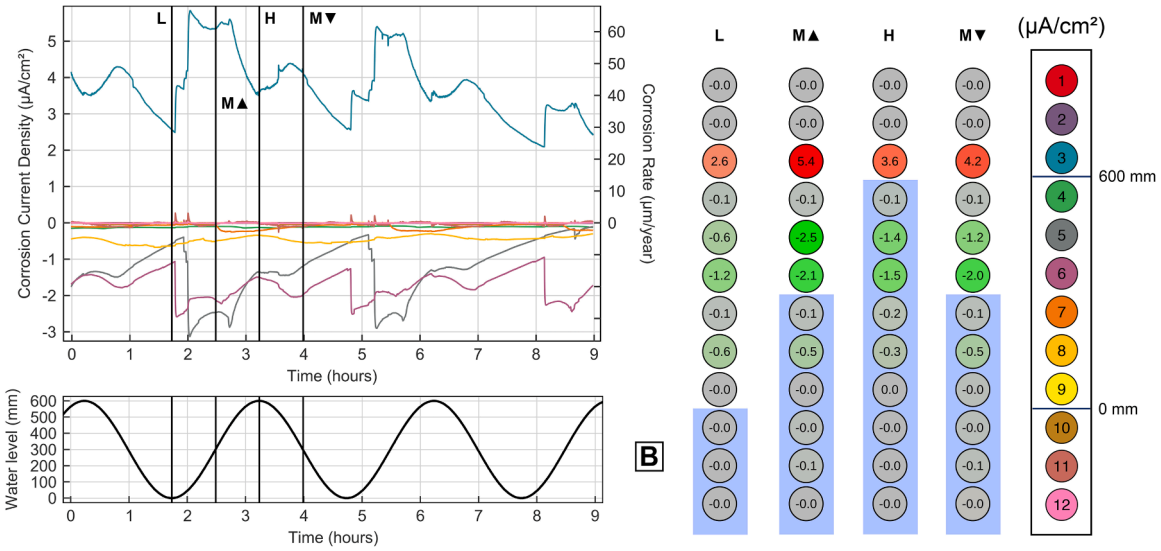

Fig. 5. Corrosion current densities on the column during the 3-hour cyclic period in the corrosion initiation stage. Water level is displayed below the corrosion current density graph, and lines labelled L, M↑, M↓ and H represent the 4 characteristic states of water level: the bottom position (L), middle positions (M↑ and M↓) and top position (H). On the right side of the graph, anodic and cathodic currents for each of these states are presented in array form.

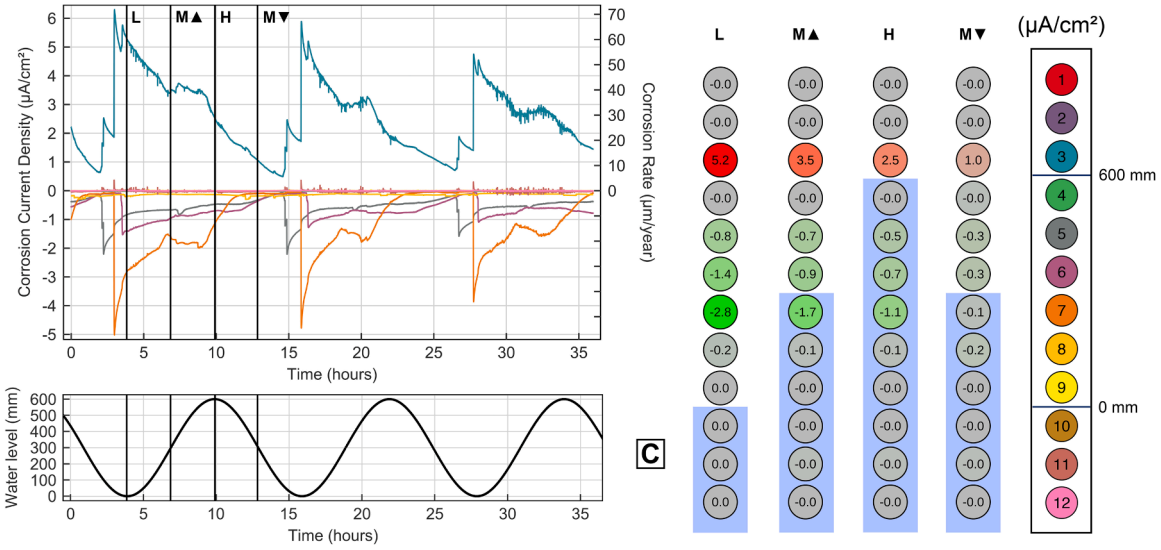

Fig. 6. Corrosion current densities on the column during the 12-hour cyclic period in the active corrosion stage. Water level is displayed below the corrosion current density graph, and lines labelled L, M↑, M↓ and H represent the 4 characteristic states of water level: the bottom position (L), middle positions (M↑ and M↓) and top position (H). On the right side of the graph, anodic and cathodic currents for each of these states are presented in array form.

Exposure during the drying period

For the last exposure period, the column was lifted out of the water basin and left to airdry for 8 weeks. The goal of this exposure was to see how anodic and cathodic reactions behave during continuous drying. Fig. 7 shows two excerpts of the anodic and cathodic currents over time, which was taken from section D and section E in Fig. 2. The result for section D (left graph) show that electrode 7 was anodic, while electrode 3 was cathodic during this part of the exposure. Anodic and cathodic contributions of other electrodes were virtually non-existent. When observing section E (right graph) at the beginning, electrodes 7 and 3 were still anodic and cathodic, respectively. During the 18th week, however, both electrodes started transitioning to cathodic behaviour, while electrode 11 became increasingly anodic over time. As previously, anodic and cathodic contributions of other electrodes were negligible.

Chloride content

Table 3 shows chloride concentrations at different electrode positions. The chloride concentration had the highest value at the position 3 electrode, which represents the area just above the highest tide level. The chloride concentration here is 0.54 %, which is about double the value of chlorides between electrodes 5 and 12. Chlorides were likely deposited in the electrode 3 position due to capillary suction when the simulated tiding reached the highest point.

Post-exposure examination

The electrodes were examined using a microCT scanner to measure the volume damaged by corrosion and to visualise the type of corrosion damage. The damaged electrodes are shown in Fig. 8 (labelled 1 to 12), and the calculated average and maximum corrosion damage, corrosion

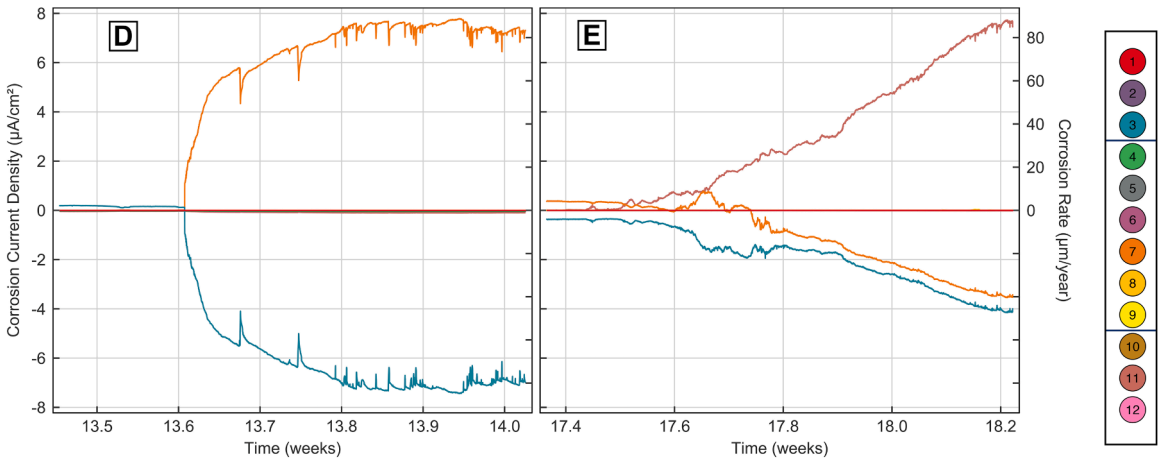

Fig. 7. Corrosion current densities on the column during the drying period. Section D is displayed on the left, and section E is displayed on the right.

Table 3
Total chloride content (by cement weight in %) at different electrode positions.

Electrode	3	5	7	9	10	12
Chloride concentration (%)	0.54	0.25	0.27	0.26	0.26	0.23

rates and ratios are shown in Table 4 and Table 5, respectively. The percentage of macrocell and microcell corrosion was calculated by comparing microCT damage and CME damage, with the results shown in Fig. 8. The microCT damage represents the total damage from both macrocell and microcell effects, while the CME represents macrocell corrosion directly (calculated by integrating anodic currents throughout the exposure period). By subtracting the CME measured damage from microCT damage, we also obtained the microcell corrosion damage. The corrosion products on electrodes 3, 5, 7 and 11 were also analysed using SEM and RAMAN analysis. The results are shown in Fig. 9, where the SEM images are labelled with uppercase letters A to D and the RAMAN spectra with lowercase letters a to d.

MicroCT results showed a mixture of damaged electrodes (e.g. 2, 3, 4, 5 and 7) and almost undamaged electrodes (e.g. 1, 6, 8 and 10). While the undamaged electrodes behaved mostly cathodic or neutral throughout the different observed exposure periods, the damaged electrodes displayed either both anodic and cathodic behaviour (electrodes 3 and 7), or were lightly cathodic or neutral (electrodes 2, 4 and 5). The latter phenomenon indicates that mostly microcell corrosion (self-corrosion) is present, which is indicated in Fig. 8. Electrodes 2, 9 and 12 also had heavy microcell corrosion present, but the amount of damage was an order of magnitude smaller compared to electrodes 2, 4 and 5. Electrodes 3, 7 and 11 exhibited a smaller portion of microcell corrosion damage (Fig. 8), likely due to forming an anode-cathode pair during the 12-hour cyclic exposure period or the drying period.

On electrode 3, where 39 % self-corrosion was identified, the corrosion products that formed at the surface of the electrode were very versatile (Fig. 9A and 9a). Flat patches merge into surfaces with fine distributed tiny corrosion products, while round formed structures are accompanied by star like features. Using Raman spectroscopy, magnetite Fe_3O_4, akageneite β-FeOOH, goethite α-FeOOH and haematite α-Fe_2O_3 were identified.

On electrode 5, where 100 % self-corrosion was identified, the observed morphology of the surface products was more even, with flat formations, cracked at some areas and with smaller areas of star like products (Fig. 9B). Here, akaganeite β-FeOOH was identified at many locations, while also goethite α-FeOOH and haematite α-Fe_2O_3 were found (Fig. 9b). These two forms of corrosion products usually coexist in a Raman spectrum.

In the third SEM image of the surface of electrode 7 (Fig. 9C), where 75 % self-corrosion was identified, the surface consists of two different areas: flat even surfaces that are cracked at some areas, and areas with 20 −30 μm long formations of lamina type of products. Here, goethite α-FeOOH, heamatite α-Fe_2O_3 and akaganeite β-FeOOH was identified by Raman spectroscopy (Fig. 9c). On electrode 11, where only 3 % self-corrosion was identified, the morphology of corrosion products was different. The presented surface of SEM image (Fig. 9D) shows round flat patches of goethite α-FeOOH and maghemite γ-Fe_2O_3. The later product was not found on electrodes, where higher percentage of self-corrosion was present. At some locations, lepidocrocite γ-FeOOH was identified by Raman spectra (Fig. 9d), which was also not found on other analysed electrodes (3, 5 and 7).

SEM investigation and Raman analysis showed that corrosion products that formed on electrodes have relation to the intensity of self-corrosion. Namely, electrodes close to 100 % self-corrosion had corrosion products with more akaganeite β-FeOOH, while on electrode with only 3 % self-corrosion, more goethite α-FeOOH and maghemite γ-Fe_2O_3 was found.

Discussion

Analysis of the corrosion damage after exposure revealed that the corrosion damage pattern along the height of the column was generally consistent with more recent understanding of corrosion processes during tidal cycles [41]. Intuitively, one would expect the greatest damage in the middle of the tidal zone, forming an asymmetric Gaussian-like pattern [16,51], as this area experiences the most extreme wet/dry cycling, with water and oxygen intake each accounting for about 50 % of the cycle duration. However, recent studies have shown that the splash zone (or upper tide level in our case) accumulates the most damage when exposed to real marine environments [41]. In our study, the highest corrosion damage on a single electrode was observed in the middle of the tidal zone (Table 4, microCT, electrode 7), but the largest group of the most corroded electrodes was found at the upper level of the tidal zone (from most to least damaged electrodes, based on Fig. 8 microCT results: 5, 4, 3, 2). The upper and lower parts of the tidal zone are more evenly exposed, being either dry or wet for most of the tidal cycle. It is this uneven wet-dry exposure that appears to create the most favourable conditions for corrosion initiation and propagation. Other authors have attributed this behaviour to greater oxygen availability due to longer drying periods [42] and higher chloride concentrations resulting from salt deposition [52]. Both scenarios seem likely in our case as well, but a fully developed transport model would be required to confirm this mechanism for our study.

It can be observed that on electrode 3 (located directly above the tidal zone), macrocell corrosion played an important role, contributing

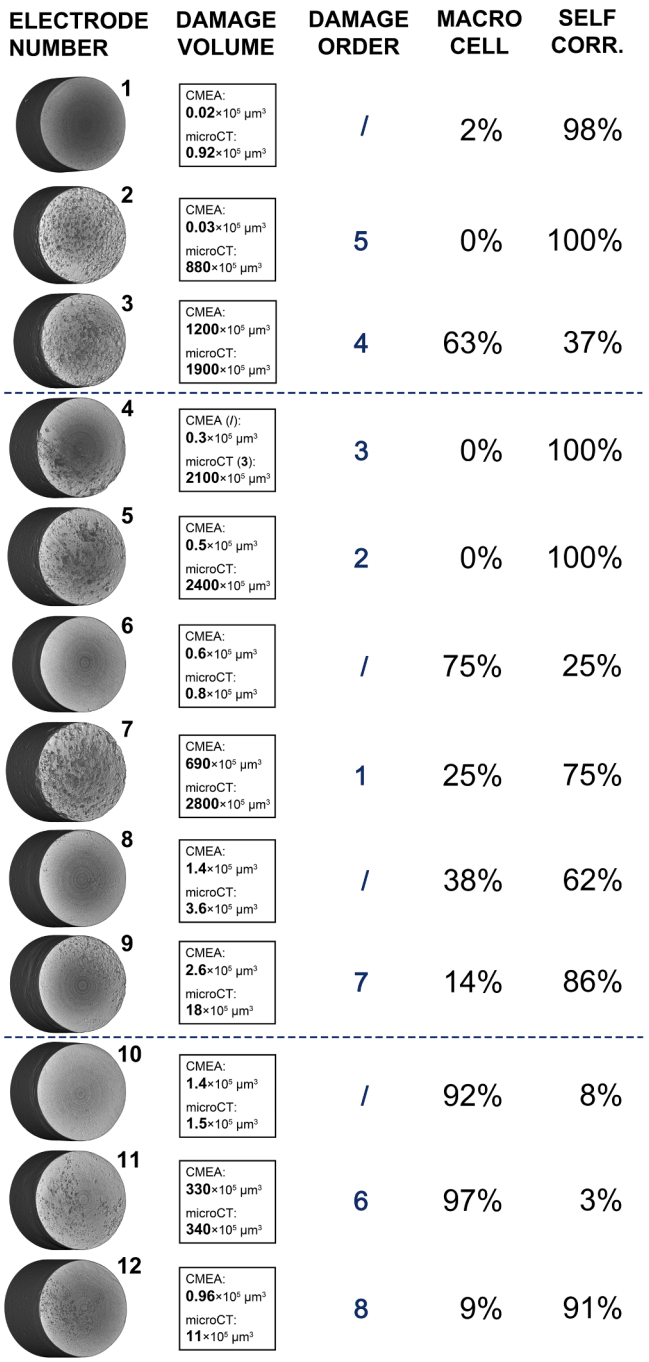

Fig. 8. Corrosion damage on each electrode (labelled 1 to 12) obtained at the end of the exposure. Square rectangles next to the electrodes show the following properties for each electrode: corrosion damage calculated from CME technique (μm^3), corrosion damage obtained from the microCT technique (μm^3). Dark blue numbers next to the squares represent the order of total damage, from most to least corroded electrode. Macrocell and self-corrosion columns represent the percentage of total corrosion damage that each type of corrosion represents.

to approximately 60 % of the total corrosion damage. On the nearby electrodes 2, 4, and 5, only microcell corrosion was present. This suggests that the conditions around the upper tidal area promote microcell corrosion, while macrocell corrosion can occur and significantly increase corrosion activity, but is not necessary to cause significant corrosion damage. The upper tidal results contrast with those for submerged electrodes, where both electrodes 10 and 11 required macrocoupling to other electrodes to sustain corrosion damage. Electrode 12

Table 4
Damage and corrosion rates calculated from CT measurements for each electrode. Average damage (Damage avg.) and average corrosion rate (v_{corr} avg.) represent corrosion activity averaged across the entire surface area of the electrode, while maximum damage (Damage max.) and maximum corrosion rate (v_{corr} max.) represent corrosion activity on the most damaged part of the electrode.

Electrode	microCT				
	Damage avg. (µm)	**v_{corr} avg. (µm/year)**	**Damage max. (µm)**	**V_{corr} max. (µm/year)**	**Ratio max./avg.**
1	-	-	-	-	-
2	3.1	8.7	410	1150	132
3	6.7	18.8	190	530	28
4	7.4	20.8	560	1570	75
5	8.5	23.9	1840	5160	216
6	-	-	-	-	-
7	9.9	27.8	880	2470	89
8	-	-	-	-	-
9	0.1	0.3	630	1770	5900
10	-	-	-	-	-
11	1.2	3.4	270	760	224
12	0.1	0.3	1050	2950	9833

Table 5
Damage, corrosion rates, anodic activity and cathodic activity calculated from CME measurements for each electrode.

Electrode	CME			
	Damage avg. (µm)	**v_{corr} avg. (µm/year)**	**Anodic activity (µA/cm²)**	**Cathodic activity (µA/cm²)**
1	-	-	-	-
2	< 0.1	< 0.1	-	0.01
3	4.1	11.4	1.00	0.72
4	-	-	-	0.03
5	-	-	-	0.16
6	-	-	-	0.20
7	2.4	6.8	0.60	0.54
8	-	-	-	0.07
9	< 0.1	< 0.1	-	0.03
10	-	-	-	0.04
11	1.2	3.3	0.28	0.06
12	< 0.1	< 0.1	-	0.02

is an outlier and was likely damaged during the drying period, when conditions for self-corrosion were present. Surprisingly, electrodes 6 and 8, the closest neighbours of the most corroded electrode 7, showed almost no corrosion damage, even though they are positioned in the middle of the tidal zone. The only possible explanation is that the most corroded electrode 7 cathodically protected its nearest neighbours. SEM and Raman analysis further validated our interpretation of CME and microCT results, as they showed that microcell electrodes exhibited predominantly general corrosion (a flat, even surface), while macrocell electrodes displayed more uneven corrosion, with laminar types of corrosion products. These results are generally comparable to other studies [53]. It appears that macrocell corrosion generated specific unstable corrosion products, such as maghemite and lepidocrocite, which were not found in the case of microcell corrosion. On most electrodes, both types of corrosion processes appeared simultaneously, so these observations should be interpreted with caution.

Microcell corrosion, as part of the overall corrosion damage, was evaluated using microCT scans only after the exposure ended. Therefore, it is uncertain when microcell corrosion initiated and developed on individual electrodes. As optimum conditions for corrosion are reached locally earlier than over larger lateral dimensions, it is assumed that microcell corrosion began before macrocell corrosion. Corrosion of the microcells probably started in the upper part of the tidal zone (electrodes 4–7) and slightly later directly above it (electrodes 2 and 3) due to

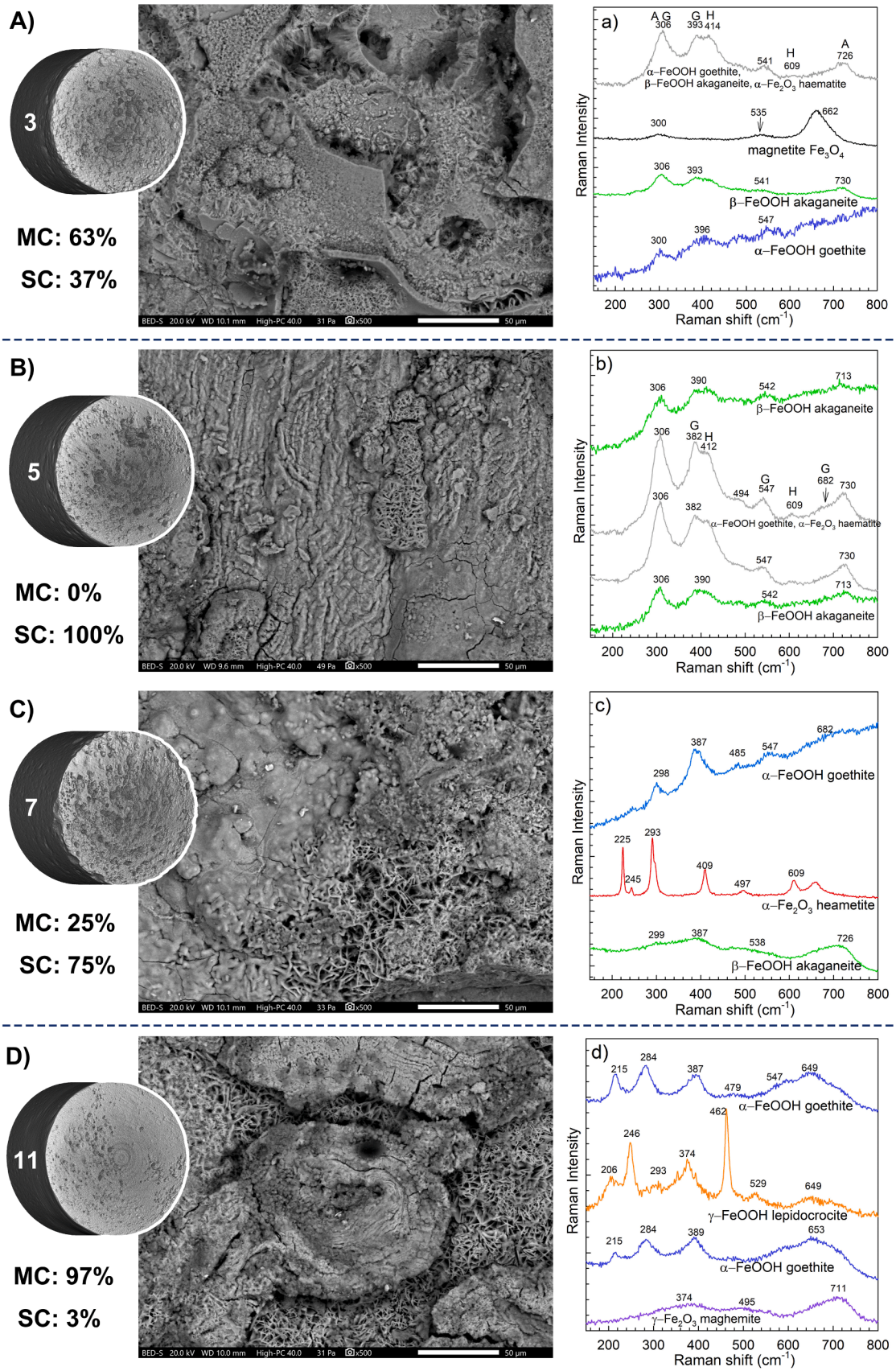

Fig. 9. Damaged electrodes and SEM images of morphology of corrosion products (labelled with capital letters A to D) and RAMAN spectra of corrosion products (labelled with lowercase letters a to d) for electrodes 3, 5, 7 and 11. The percentage of macrocell (MC) and self-corrosion (SC) is also indicated.

capillary suction of water. The growth of corrosion products most likely accelerated the development of macrocell corrosion between electrodes. The role of corrosion products is not exactly known, but they likely reduce the polarization resistance between specific electrode pairs (due to reduced Rp at individual electrodes) or may even participate in electrochemical reactions. This phenomenon could also explain the anode–cathode switching of electrodes 3 and 7 during drying. To gain a comprehensive understanding of these combined corrosion processes, simultaneous monitoring of microcell and macrocell corrosion on all electrodes is needed. Such an approach would probably also provide specific information to explain how initial corrosion damage and subsequent corrosion products determine the further evolution of corrosion processes.

Macrocell corrosion under simulated tidal conditions showed a notably complex pattern. During the incubation stage (weeks 1 to 7), the most anodic electrode was located in the middle of the tidal zone (7), while the submerged electrodes (10, 11 and 12) acted as cathodes. During this period, most signals followed a sinusoidal pattern, with the lowest and highest corrosion activity directly corresponding to the lowest and highest tide levels. An offset was also observed in most of the measured currents, as the currents did not oscillate around zero. Towards the end of the 3-hour cycles (week 8), macrocell current signals changed from a sinusoidal pattern to a switch-on/switch-off type. It is assumed that this transition marked the onset of active corrosion. Typical amplitudes increased by two orders of magnitude: from approximately 42 ± 6 nA/cm^2 during the incubation phase to 6.3 ± 0.4 μA/cm^2 during active corrosion. The electrode just above the tidal zone (3) became the most anodic, while the electrodes in the middle of the tidal zone (5, 6, 7) switched to cathodic activity. As corrosion processes further developed in the second part of the exposure, the switch-on/switch-off type of measured macrocell current became more pronounced, while the DC component of the signals decreased. The peak currents coincided with the lowest water level, which was the opposite of the earlier exposure period. It is not entirely clear what effect the applied frequencies (1/3 h^{-1}, 1/12 h^{-1}) had on the overall corrosion processes, but apparently even the lower frequency of 1/12 h^{-1} was still too high to achieve complete drying of the concrete and oxygen ingress. This could partly explain why the cathode was located in water or the tidal zone during our experiment. On the other hand, it is uncertain to what extent the applied frequencies can be related to real tidal conditions, as the dimensions of the test specimen (10 mm concrete cover, cross-section of 64 cm^2) are smaller than those commonly used in marine concrete structures (at least 50 mm concrete cover).

It can be observed that certain anode-cathode pairs persisted throughout the entire measurement. The maximum macrocell current was usually measured between anodes and cathodes separated by a few (3–5) electrodes, while the current measured between other electrodes was lower. An attempt to explain this behaviour was made for the drying phase, where this phenomenon was particularly noticeable. Once the entire column was lifted out of the water, the concrete began to dry on all sides. Due to the vertical position of the column, the water inside likely migrated downwards, increasing oxygen availability behind the primary waterfront. At the very beginning of the drying process, electrode 3 was still the anode and electrodes 7 and 11 were the cathode. Later during drying, the electrode in the centre of the column (7) became the anode, and the electrode further up the column (3) became the cathode. Surprisingly, the other electrodes did not participate in the macrocell current exchange. During the second part of drying, the electrode at the bottom of the column (11) became the anode, while the middle electrode (7) changed from anode to cathode. Electrode 3 remained a cathode, with two observed peaks during the drying period. These changes in anode-cathode pairs during the downward movement of the main waterfront are logical: the anode was in front of the waterfront, and the cathode was behind it. However, it is not entirely clear why the anode-cathode pairs are exactly four electrodes apart, and the electrodes in between showed almost no activity. It is assumed that one reason for this phenomenon was cathodic protection of the nearby electrodes by the predominant anode, combined with the availability of oxygen at individual electrodes and electrical conductivity between the electrodes.

The role of corrosion products in influencing anode–cathode pairs remains unclear, but they likely contributed to their formation, with the most anodic electrodes also acting as the most cathodic. It is known that soluble or porous products can accelerate anodic reactions due to reduced repassivation ability [54]. Recently, the role of corrosion products under cathodic protection was described [55]. Comparing observations obtained under cathodic protection with those from a free corrosion environment may be questionable; however, our results indicate a clear correlation between the most anodic and the most cathodic electrodes (Table 5).

In a research study by J.R. Scully, J.L. Hudson, and other co-authors [56], it was established that anodic and cathodic sites interact, and that the main processes involved are either diffusion (activating), oxide film weakening (activating), or Ohmic potential drop (inhibiting). A similar observation was described by Elsener and co-authors [57], who investigated the distribution of cathodic current near the main anodic area; however, the mutual effect of multiple anodic sites was not considered. The diffusion of corrosion products was also not considered, as these are presumed not to significantly influence the arrangement of anodic and cathodic sites in a porous material such as concrete. It is believed that the combination of Ohmic potential drop and passivity could play a significant role in the formation of anode-cathode pairs across the three to four electrodes indicated in our results. This phenomenon requires more attention in future studies.

This study also has several limitations that should be acknowledged. The results are based on a single experimental specimen, and therefore the findings should be interpreted as exploratory rather than statistically generalisable. The concrete used had a high water-to-cement ratio and a relatively thin cover depth, which may accelerate moisture and ion-transport effects compared with typical structural elements found in marine environments. Furthermore, key environmental variables such as oxygen availability and moisture were not directly measured but implied based on the water level position. This limited our ability to quantify the coupled moisture–oxygen transport processes that likely influenced the corrosion behaviour. These constraints do not diminish the value of the observed trends but highlight the need for additional studies and more comprehensive measurements in future work.

Our findings obtained

Conclusions

Macrocell corrosion currents were measured using coupled multi-electrodes (CMEs) during simulated tidal conditions. Continuous changes in water level produced repeating patterns in the measured signals, although some long-term drift effects were also observed.

- Coupled multi-electrodes were successfully used to monitor the evolution of macrocell corrosion under simulated tidal conditions. Changes in current patterns were detected as a result of cyclic water level changes, shifting from sinusoidal to switch-like behaviour as corrosion progressed.
- Anodic and cathodic macrocell currents were highest when the water level was at its lowest position during active corrosion. Anodic and cathodic pairs developed, consistently separated by several electrodes, with intermediate electrodes often remaining inactive.
- Damage analysis showed significant contributions from both macrocell and microcell corrosion. Microcell corrosion was present on several electrodes, particularly in the high-tide area, while macrocell corrosion caused damage as specific anode–cathode pairs across all exposure zones.
- Corrosion damage did not follow an uneven Gaussian vertical distribution. Instead, it was influenced by dynamic wetting patterns and

electrode interactions. Electrodes in the high-tide zone exhibited the most extensive group damage.
- SEM and Raman analysis showed that general corrosion and stable oxide phases were observed on electrodes with predominantly microcell corrosion, whereas macrocell corrosion resulted in more uneven damage and the formation of less stable products such as maghemite and lepidocrocite.

To fully understand these combined corrosion processes, especially the interaction between microcell and macrocell corrosion, further research using a comprehensive monitoring approach is required. In particular, the application of multiple simultaneous monitoring techniques capable of capturing both microcell and macrocell corrosion activity is needed to obtain a complete and accurate picture of the underlying corrosion mechanisms.

Funding and acknowledgements

The authors acknowledge the financial support from the Slovenian Research Agency (research core funding No P2–0273).

The authors would like to thank Viljem Kuhar for his help in preparing and designing the specimens.

CRediT authorship contribution statement

Miha Hren: Writing – review & editing, Writing – original draft, Visualization, Validation, Software, Resources, Project administration, Methodology, Investigation, Data curation, Conceptualization. **Tadeja Kosec:** Writing – review & editing, Visualization, Supervision, Project administration, Conceptualization. **Andraž Legat:** Writing – review & editing, Writing – original draft, Supervision, Project administration, Methodology, Funding acquisition, Conceptualization.

Declaration of competing interest

The authors declare that they have no known competing financial interests or personal relationships that could have appeared to influence the work reported in this paper.

Supplementary materials

Supplementary material associated with this article can be found, in the online version, at doi:10.1016/j.electacta.2025.148026.

Data availability

Data will be made available on request.

References

[1] L. Bertolini, B. Elsener, P. Pedeferri, E. Redaelli, R.B. Polder, Corrosion of Steel in Concrete: Prevention, Diagnosis, Repair, Wiley-VCH Verlag GmbH & Co., Weinheim, Germany, 2013. http://doi.wiley.com/10.1002/9783527651696. accessed July 8, 2016.
[2] ed.H. Böhni (Ed.), Corrosion in Reinforced Concrete Structures, CRC Press, Cambridge, England: Boca Raton, 2005.
[3] J.P. Broomfield, Corrosion of Steel in Concrete: Understanding, Investigation and Repair, CRC Press, 2006. Second Edition.
[4] J.P. Broomfield, Corrosion of Steel in Concrete : Understanding, Investigation and Repair, Taylor & Francis, London, UK, 2003. Second Edition, https://www.taylorfrancis.com/books/9781482265491. accessed August 28, 2018.
[5] C. Alonso, C. Andrade, J.A. González, Relation between resistivity and corrosion rate of reinforcements in carbonated mortar made with several cement types, Cem. Concr. Res. 18 (1988) 687–698, https://doi.org/10.1016/0008-8846(88)90091-9.
[6] R. Rodrigues, S. Gaboreau, J. Gance, I. Ignatiadis, S. Betelu, Reinforced concrete structures: a review of corrosion mechanisms and advances in electrical methods for corrosion monitoring, Constr. Build. Mater. 269 (2021) 121240, https://doi.org/10.1016/j.conbuildmat.2020.121240.
[7] J. Taheri-Shakib, A. Al-Mayah, Effect of corrosion pit distribution of rebar on pore, and crack characteristics in concrete, Cem. Concr. Compos. 148 (2024) 105476, https://doi.org/10.1016/j.cemconcomp.2024.105476.
[8] J. Wang, Q. Wang, Y. Zhao, P. Li, T. Ji, G. Zou, Y. Qiao, Z. Zhou, G. Wang, D. Song, Research progress of macrocell corrosion of steel rebar in concrete, Coatings 13 (2023) 853, https://doi.org/10.3390/coatings13050853.
[9] C. Chalhoub, R. François, M. Carcasses, Effect of cathode–Anode distance and electrical resistivity on macrocell corrosion currents and cathodic response in cases of chloride induced corrosion in reinforced concrete structures, Constr. Build. Mater. 245 (2020) 118337, https://doi.org/10.1016/j.conbuildmat.2020.118337.
[10] S. Sathiyanarayanan, P. Natarajan, K. Saravanan, S. Srinivasan, G. Venkatachari, Corrosion monitoring of steel in concrete by galvanostatic pulse technique, Cem. Concr. Compos. 28 (2006) 630–637, https://doi.org/10.1016/j.cemconcomp.2006.03.005.
[11] Ø. Vennesland, M. Raupach, C. Andrade, Recommendation of Rilem TC 154-EMC: "electrochemical techniques for measuring corrosion in concrete"—Measurements with embedded probes, Mater. Struct. 40 (2007) 745–758, https://doi.org/10.1617/s11527-006-9219-4.
[12] P.V. Nygaard, M.R. Geiker, B. Elsener, Corrosion rate of steel in concrete: evaluation of confinement techniques for on-site corrosion rate measurements, Mater. Struct. 42 (2009) 1059–1076, https://doi.org/10.1617/s11527-008-9443-1.
[13] A. Fahim, P. Ghods, O.B. Isgor, M.D.A. Thomas, A critical examination of corrosion rate measurement techniques applied to reinforcing steel in concrete, Mater. Corros (2018), https://doi.org/10.1002/maco.201810263.
[14] S. Qian, J. Zhang, D. Qu, Theoretical and experimental study of microcell and macrocell corrosion in patch repairs of concrete structures, Cem. Concr. Compos. 28 (2006) 685–695, https://doi.org/10.1016/j.cemconcomp.2006.05.010.
[15] Mansfeld, Classic paper in Corrosion Science and Engineering with a perspective by F. Mansfeld, Corrosion 62 (2006) 843–855, https://doi.org/10.5006/1.3279894.
[16] J.R. Lliso-Ferrando, J. Soto, I. Gasch, M. Valcuende, Significance of macrocell currents in reinforced concrete columns partially immersed in seawater, Constr. Build. Mater. 389 (2023) 131739, https://doi.org/10.1016/j.conbuildmat.2023.131739.
[17] U.M. Angst, M.R. Geiker, A. Michel, C. Gehlen, H. Wong, O.B. Isgor, B. Elsener, C. M. Hansson, R. François, K. Hornbostel, R. Polder, M.C. Alonso, M. Sanchez, M. J. Correia, M. Criado, A. Sagüés, N. Buenfeld, The steel–concrete interface, Mater. Struct 50 (2017), https://doi.org/10.1617/s11527-017-1010-1.
[18] A.A. Sagüés, M.A. Pech-Canul, A.K.M. Shahid Al-Mansur, Corrosion macrocell behavior of reinforcing steel in partially submerged concrete columns, Corros. Sci. 45 (2003) 7–32, https://doi.org/10.1016/S0010-938X(02)00087-2.
[19] U. Angst, M. Büchler, On the applicability of the Stern–Geary relationship to determine instantaneous corrosion rates in macro-cell corrosion, Mater. Corros. 66 (2015) 1017–1028, https://doi.org/10.1002/maco.201407997.
[20] J.Y. Hu, S.S. Zhang, E. Chen, W.G. Li, A review on corrosion detection and protection of existing reinforced concrete (RC) structures, Constr. Build. Mater. 325 (2022) 126718, https://doi.org/10.1016/j.conbuildmat.2022.126718.
[21] A. Fraundorfer, C. Dauberschmidt, C. Gehlen, Approach to consider self-corrosion in corrosion monitoring of reinforced concrete structures exposed to chlorides, Mater. Corros. 75 (2024) 516–528, https://doi.org/10.1002/maco.202314115.
[22] A. Brenna, L. Lazzari, M. Ormellese, Monitoring chloride-induced corrosion of carbon steel tendons in concrete using a multi-electrode system, Constr. Build. Mater. 96 (2015) 434–441, https://doi.org/10.1016/j.conbuildmat.2015.08.037.
[23] A. Česen, T. Kosec, A. Legat, Characterization of steel corrosion in mortar by various electrochemical and physical techniques, Corros. Sci. 75 (2013) 47–57, https://doi.org/10.1016/j.corsci.2013.05.015.
[24] G.S. Duffó, S.B. Farina, Development of an embeddable sensor to monitor the corrosion process of new and existing reinforced concrete structures, Constr. Build. Mater. 23 (2009) 2746–2751, https://doi.org/10.1016/j.conbuildmat.2009.04.001.
[25] A. Legat, Monitoring of steel corrosion in concrete by electrode arrays and electrical resistance probes, Electrochim. Acta 52 (2007) 7590–7598, https://doi.org/10.1016/j.electacta.2007.06.060.
[26] M. Hren, T. Kosec, A. Legat, Characterization of stainless steel corrosion processes in mortar using various monitoring techniques, Constr. Build. Mater. 221 (2019) 604–613, https://doi.org/10.1016/j.conbuildmat.2019.06.120.
[27] M. Laleh, Y. Huo, R.E. Melchers, M.Y. Tan, Electrode array probe designed for visualising and monitoring multiple localised corrosion processes and mechanisms simultaneously occurring on marine structures, Npj Mater. Degrad. 7 (2023) 68, https://doi.org/10.1038/s41529-023-00388-9.
[28] M. Hren, T. Kosec, A. Legat, An investigation into corrosion around voids at the steel-concrete interface, Cem. Concr. Res. 181 (2024) 107545, https://doi.org/10.1016/j.cemconres.2024.107545.
[29] M. Hren, T. Kosec, A. Legat, Characterization of steel corrosion processes in various blended cements by means of coupled multi-electrode arrays, Cem. Concr. Res. 168 (2023) 107134, https://doi.org/10.1016/j.cemconres.2023.107134.
[30] M. Hren, T. Kosec, M. Lindgren, E. Huttunen-Saarivirta, A. Legat, Sensor development for corrosion monitoring of stainless steels in H2SO4 solutions, Sensors 21 (2021) 1449, https://doi.org/10.3390/s21041449.
[31] N. Gartner, T. Kosec, A. Legat, Monitoring the corrosion of steel in concrete exposed to a marine environment, Materials 13 (2020) 407, https://doi.org/10.3390/ma13020407.
[32] E. Rossi, R. Polder, O. Copuroglu, T. Nijland, B. Šavija, The influence of defects at the steel/concrete interface for chloride-induced pitting corrosion of naturally-deteriorated 20-years-old specimens studied through X-ray computed tomography, Constr. Build. Mater. 235 (2020) 117474, https://doi.org/10.1016/j.conbuildmat.2019.117474.

[33] X. Xi, S. Yang, Investigating the spatial development of corrosion of corner-located steel bar in concrete by X-ray computed tomography, Constr. Build. Mater. 221 (2019) 177–189, https://doi.org/10.1016/j.conbuildmat.2019.06.023.
[34] B. Dong, G. Shi, P. Dong, W. Ding, X. Teng, S. Qin, Y. Liu, F. Xing, S. Hong, Visualized tracing of rebar corrosion evolution in concrete with x-ray micro-computed tomography method, Cem. Concr. Compos. 92 (2018) 102–109, https://doi.org/10.1016/j.cemconcomp.2018.06.003.
[35] G. Fang, W. Ding, Y. Liu, J. Zhang, F. Xing, B. Dong, Identification of corrosion products and 3D distribution in reinforced concrete using X-ray micro computed tomography, Constr. Build. Mater. 207 (2019) 304–315, https://doi.org/10.1016/j.conbuildmat.2019.02.133.
[36] J. Taheri-Shakib, A. Al-Mayah, Influence of concrete cover thickness on steel corrosion in reinforced concrete: insights from advanced imaging and material analysis, Int. J. Electrochem. Sci. 20 (2025) 100933, https://doi.org/10.1016/j.ijoes.2025.100933.
[37] M. Beck, J. Goebbels, A. Burkert, B. Isecke, R. Bäßler, Monitoring of corrosion processes in chloride contaminated mortar by electrochemical measurements and X-ray tomography, Mater. Corros. 61 (2010) 475–479, https://doi.org/10.1002/maco.200905364.
[38] J. Taheri-Shakib, A. Al-Mayah, Dynamics of localized accelerated corrosion in reinforced concrete: voids, corrosion products, and crack formation, Ceram. Int. 50 (2024) 48755–48767, https://doi.org/10.1016/j.ceramint.2024.09.229.
[39] L. Bourreau, L. Gaillet, V. Bouteiller, F. Schoefs, B. Thauvin, J. Schneider, S. Naar, Spatial identification of exposure zones of concrete structures exposed to a marine environment with respect to reinforcement corrosion, Struct. Infrastruct. Eng. 16 (2020) 346–354, https://doi.org/10.1080/15732479.2019.1655072.
[40] M. Otieno, M. Thomas, 7 - Marine exposure environments and marine exposure sites (Ed.), in: M.G. Alexander (Ed.), 7 - Marine exposure environments and marine exposure sites, Mar. Concr. Struct. (2016) 171–196, https://doi.org/10.1016/B978-0-08-100081-6.00007-6.
[41] Q. Liu, Y. Chen, Y. Ge, Q. Xiong, J. Ma, Y. Wang, F. Zhang, Time-dependent non-uniform corrosion of concrete structures under marine environments considering the vertical variation of exposure conditions, Ocean Eng. 306 (2024) 118105, https://doi.org/10.1016/j.oceaneng.2024.118105.
[42] A. Moore, H. Beushausen, M. Otieno, J. Ndawula, M. Alexander, Oxygen availability and corrosion propagation in RC structures in the marine environment—Inferences from field and laboratory studies, Corros. Mater. Degrad. 3 (2022) 363–375, https://doi.org/10.3390/cmd3030022.
[43] K. Li, J. Zeng, L. Tang, H.E. Sørensen, C. Andrade, R. Maddalena, L. Huang, G. Geng, P.C. Borges, G.C. Keserle, S. Wang, F. Martirena-Hernández, F. Kanavaris, A.V. Monteiro, K. Kovler, P. Zhang, T. Bansal, T. Visalakshi, R. Torrent, RILEM recommendation from TC 289-DCM: guideline for designing and operating long-term marine exposure sites, Mater. Struct. 57 (2024) 44, https://doi.org/10.1617/s11527-024-02319-9.
[44] K. Li, J. Zeng, L. Tang, H.E. Sørensen, P.Castro Borges, M.R. Geiker, M.T. Pedersen, P. Zhang, S. Surana, R. Maddalena, J. Wang, C. Andrade, V. Baroghel-Bouny, F. Martirena-Hernández, G. Geng, K. Kovler, S. Wang, Long-term field exposure of structural concretes in marine environment: state-of-the-art review by RILEM TC 289-DCM, Mater. Struct. 55 (2022) 205, https://doi.org/10.1617/s11527-022-02027-2.
[45] H.T. Bui, K.H. Tan, Microcell and macrocell corrosion kinetics of steel bars in reinforced concrete slabs subjected to alternate wet and dry environments, Constr. Build. Mater. 426 (2024) 136181, https://doi.org/10.1016/j.conbuildmat.2024.136181.
[46] M. Hren, V. Bokan Bosiljkov, A. Legat, Effects of blended cements and carbonation on chloride-induced corrosion propagation, Cem. Concr. Res. 145 (2021) 106458, https://doi.org/10.1016/j.cemconres.2021.106458.
[47] SIST EN 12390-2:2019, Testing hardened concrete - part 2: making and curing specimens for strength tests (n.d.), https://standards.iteh.ai/catalog/standards/sist/fd, 2020, 4d81ed-0bc4-40a9-9fc0-4899eb7d5da1/sist-en-12390-2-2019 (accessed November 16, 2025).
[48] ASTM, ASTM G102-89: standard practice for calculation of corrosion rates and related information from electrochemical measurements, 2016.
[49] C. Arya, N.R. Buenfeld, J.B. Newman, Assessment of simple methods of determining the free chloride ion content of cement paste, Cem. Concr. Res. 17 (1987) 907–918, https://doi.org/10.1016/0008-8846(87)90079-2.
[50] SIST EN 14629, 2007, Products and systems for the protection and repair of concrete structures - test methods - determination of chloride content in hardened concrete, (2007).
[51] P.K. Mehta, Concrete in the Marine Environment, Elsevier Applied Science, London, New York, 1991.
[52] H. Chang, Z. Zhang, Z. Ma, Y. Ji, X. Huang, Permeation characteristics and surface accumulation of chloride in different zones of concrete along altitude in marine environments, Crystals 11 (2021) 722, https://doi.org/10.3390/cryst11070722.
[53] D. Neff, J. Harnisch, M. Beck, V. L'Hostis, J. Goebbels, D. Meinel, Morphology of corrosion products of steel in concrete under macro-cell and self-corrosion conditions, Mater. Corros. 62 (2011) 861–871, https://doi.org/10.1002/maco.201005861.
[54] U.M. Angst, E. Rossi, C. Boschmann Käthler, D. Mannes, P. Trtik, B. Elsener, Z. Zhou, M. Strobl, Chloride-induced corrosion of steel in concrete—Insights from bimodal neutron and X-ray microtomography combined with ex-situ microscopy, Mater. Struct. 57 (2024) 56, https://doi.org/10.1617/s11527-024-02337-7.
[55] F. Martinelli-Orlando, S. Mundra, U.M. Angst, Cathodic protection mechanism of iron and steel in porous media, Commun. Mater. 5 (2024) 15, https://doi.org/10.1038/s43246-024-00454-y.
[56] T.T. Lunt, J.R. Scully, V. Brusamarello, A.S. Mikhailov, J.L. Hudson, Spatial interactions among localized corrosion sites : experiments and modeling, J. Electrochem. Soc 149 (2002) B163, https://doi.org/10.1149/1.1466858.
[57] B. Elsener, Macrocell corrosion of steel in concrete – implications for corrosion monitoring, Cem. Concr. Compos. 24 (2002) 65–72, https://doi.org/10.1016/S0958-9465(01)00027-0.